*J. Synchrotron Rad.* (2000). **7**, 274–279

# A novel experimental technique for atomic X-ray holography

**B. Adams, Y. Nishino*† and G. Materlik**

*Hamburger Synchrotronstrahlungslabor HASYLAB at Deutsches Elektronen-Synchrotron DESY, Notkestrasse 85, D-22607 Hamburg, Germany. E-mail: nishino@desy.de*

(*Received 20 September 1999; accepted 17 January 2000*)

A new experimental technique for reciprocal X-ray holography has been developed. The experimental set-up makes it possible to measure a reciprocal hologram without unwanted mixture of the X-ray fluorescence holography signal. The data are recorded during continuous rotation of the sample, and are accumulated over many revolutions. Thus the sensitivity to fluctuations of the source characteristics is reduced. A very high resolution over a large angular range is also achieved, which allows recording of X-ray standing-wave shapes near Bragg angles. The reconstruction of the measured hologram of a $Cu_3Au$ crystal gives positions of the nearest and next-nearest neighbours of a fluorescing Cu atom.

**Keywords: imaging; X-ray holography; structure determination.**

## 1. Introduction

Holography with atomic resolution was first proposed by Szöke (1986) for both electrons and X-rays. This suggestion was realized for X-rays by Tegze & Faigel (1996), and called the direct method of X-ray fluorescence holography (XFH). In parallel, Gog, Len *et al.* (1996) developed and proved experimentally reciprocal X-ray holography, which was named multiple-energy X-ray holography (MEXH), since its energy range is not limited by the availability of characteristic fluorescence lines.

Both methods make use of the interference of unscattered and scattered waves, being the reference and object waves in the sense of holography. In XFH, X-ray fluorescence atoms in a stationary sample are excited by X-rays from an external source. Fluorescence photons are recorded by a detector in the far field. The fluorescence intensity is spatially modulated, because the outgoing fluorescence waves are scattered from neighbouring atoms and interfere with unscattered reference waves. In reciprocal holography, interference inside a sample is formed by the unscattered incident waves from an external X-ray source and waves scattered from neighbouring atoms. The wave field intensity at the site of a fluorescing atom is modulated when the sample is rotated with respect to the incident X-rays. This modulation is detected, for example, by recording the fluorescence intensity from this atom.

In both XFH and MEXH, X-rays are incident on a sample and fluorescence photons are measured. Interference of the incoming X-rays results in MEXH, and XFH is caused by interference of the outgoing fluorescence X-rays. The experimental set-up should ensure that the detected signal modulation comes from only the incoming side for MEXH and from only the outgoing side for XFH, as was pointed out by Novikov *et al.* (1998). A *pure* XFH measurement is carried out by fixing the sample orientation with respect to the incoming X-ray beam to keep all contributions from the incoming side static (Hiort *et al.*, 2000). In *pure* reciprocal holography the fluorescence detectors should move together with the sample so that no signal modulation comes from the outgoing side. Although pure holography is desirable, all reciprocal X-ray holography experiments reported so far (Gog, Len *et al.*, 1996; Gog, Menk *et al.*, 1996; Adams, Novikov *et al.*, 1998; Gog *et al.*, 1998; Hayashi *et al.*, 1998; Novikov *et al.*, 1998; Tegze *et al.*, 1999) have been carried out in the so-called *mixed* set-up, because it is much easier to realize. In the mixed set-up the detectors move together with the sample in only one of two independent angular motions. In this case one measures a fluorescence intensity modulation resulting both from the reciprocal hologram by the incident X-rays

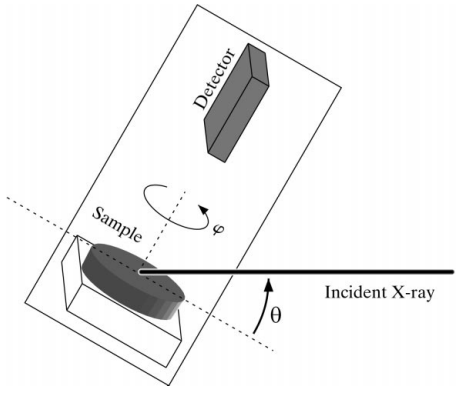


**Figure 1**
Experimental set-up.

† On leave from Japan Synchrotron Radiation Research Institute (JASRI), 1-1-1 Kouto, Mikazuki-cho, Sayo-gun, Hyogo 679-5198, Japan.

and from the direct hologram by the outgoing fluorescence X-ray. In order to obtain a pure reciprocal hologram, one has to subtract the direct hologram signal from the measured mixed hologram (Novikov *et al.*, 1998; Tegze *et al.*, 1999; Adams *et al.*, 1999). This subtraction procedure may disturb reconstructed atomic images.

In the set-up for pure reciprocal holography there has been a difficulty of limited angular range, because the detectors must not cast a shadow on the sample. It is, however, possible to keep a wide angular range in pure reciprocal holography, *e.g.* by putting the sample inside a proportional electron counter, such as when Korecki *et al.* (1997, 1999) measured the conversion electron intensity from pure reciprocal 'Mössbauer' holography. In this paper we report another reciprocal holography experiment scheme.

For crystalline samples, features appearing in the XFH and MEXH holograms are interpreted as Kossel lines and X-ray standing waves (XSWs), respectively (Gog *et al.*, 1995; Adams, Novikov *et al.*, 1998). Our experimental set-up makes it possible, in addition, to measure XSW shapes near Bragg angles, and thus opens the way to simultaneously collect information about long-range order in the structure (Bedzyk & Materlik, 1985).

## 2. Experiment

The experiment was carried out at the bending-magnet beamline CEMO of the Hamburg Synchrotron Radiation Laboratory (HASYLAB) with a toroidally focusing mirror and a Si(111) double-crystal monochromator set to 10.5 keV. We performed a reciprocal holography measurement on a $Cu_3Au$ single-crystal sample with a (001) surface. It has a face-centred-cubic (f.c.c.)-based structure with a lattice constant of 3.75 Å. The $K\alpha$ (8.0 keV) and $K\beta$ (8.9 keV) fluorescence lines of Cu atoms were measured.

Fig. 1 shows the experimental set-up. A rotation stage ($\varphi$ stage) and a Si drift detector are mounted on a diffractometer circle with the horizontal rotation axis perpendicular to the incident beam ($\theta$ axis). The sample is mounted on the $\varphi$ stage with its surface normal parallel to the $\varphi$ axis.

Both the sample and the detector rotate in $\theta$, but only the sample rotates in $\varphi$. The detector has its entrance window on the $\varphi$ axis. Assuming that the detector efficiency is rotationally symmetric about the $\varphi$ rotation axis, this set-up is equivalent to the pure reciprocal holography set-up, where the detector rotates together with the sample in both $\theta$ and $\varphi$.

The sample rotates in $\varphi$ at a constant speed of 0.05 revolutions per second. Fluorescence photons are counted during the rotation. The counts are stored in angle-proportional memory locations of a histogramming memory at an angular resolution of 0.006° in $\varphi$. For each position of $\theta$ the detector counts are added up over 180 revolutions in $\varphi$. Thus the sensitivity to fluctuations of the source characteristics is reduced. Holography measurement with continuous rotation of a sample is much more efficient than the standard method of moving in small steps and counting between the steps. This approach was first reported by Adams, Hiort *et al.* (1998), and the importance was stressed in a review article by Faigel & Tegze (1999). A fine angular resolution makes it possible to measure XSW shapes near Bragg angles.

The data acquisition is controlled by a custom-made digital circuit implemented in a programmable logic array and connected to a PC. It produces stepping-motor pulses for the $\varphi$ rotation and sorts the detector counts into $\varphi$-proportional channels of a 20 bit-wide 32 bit-deep histogramming memory.

## 3. Analysis

The original data contain 60000 $\varphi$ points in $2\pi$, and $\theta$ ranges from 31° to 73° in 1° steps. Since such a high angular resolution in $\varphi$ is not necessary for the holographic reconstruction, we first add 150 adjacent $\varphi$ data points. After the compression of the data the Cu fluorescence counts for each data point become $\sim 1 \times 10^5$. The resulting atomic images with this compression rate are similar to those with a lower data compression rate, *e.g.* of adding ten adjacent $\varphi$ data points (not shown).

The measured fluorescence intensity is composed of the reference wave and the object wave,

$$\begin{aligned} I(\mathbf{k}) &= |R(\mathbf{k}) + O(\mathbf{k})|^2 \\ &= |R(\mathbf{k})|^2 + 2\mathrm{Re}[R^*(\mathbf{k})O(\mathbf{k})] + |O(\mathbf{k})|^2, \end{aligned} \quad (1)$$

where $R(\mathbf{k})$ is the amplitude of the reference wave, $O(\mathbf{k})$ is the amplitude of the object waves and $\mathbf{k}$ is the incident X-ray wavevector. The holographic information is contained in the interference term $2\mathrm{Re}[R^*(\mathbf{k})O(\mathbf{k})]$, and the normalized hologram $\chi(\mathbf{k})$ is obtained from

$$\chi(\mathbf{k}) \simeq [I(\mathbf{k}) - I_0(\mathbf{k})]/I_0(\mathbf{k}), \quad (2)$$

where $I_0(\mathbf{k}) = |R(\mathbf{k})|^2$. Here we assume that the interference term is much smaller than the reference term $|R(\mathbf{k})|^2$, and the square of the object waves $|O(\mathbf{k})|^2$ is negligible. This assumption is correct for $\mathbf{k}$ far from Bragg angles. For $\mathbf{k}$ close to a Bragg angle, the waves scattered from all crystal atoms contribute constructively and produce a strong XSW field inside the sample, and thus the square of the object waves may become non-negligible. This makes the extraction of the normalized hologram $\chi(\mathbf{k})$ from the measured fluorescence intensity $I(\mathbf{k})$ rather difficult near Bragg angles. For this reason we later exclude the data near Bragg angles from the holographic analysis.

$I_0(\mathbf{k})$ has an angular dependence due to changing absorption conditions of the incoming X-ray and outgoing fluorescence. In order to include the absorption effect in the determination of $I_0(\mathbf{k})$, we fitted the data with a function $I_0 = a_1 + a_2 \sin\varphi + a_3 \cos\varphi$ for each $\theta$ (one-dimensional fitting), where $a_1$, $a_2$ and $a_3$ are fit parameters. The oscillation of $I_0$ in $\varphi$ is possibly caused by a misalignment of

the sample and by a photoelectron interaction with neighbour atoms (Nishino & Materlik, 1999).

The obtained $\chi(\mathbf{k})$ contains peaks near Bragg angles. In order to eliminate these peaks the data, which deviate from $I_0$ by more than 1%, are set to $I_0$. The total number of eliminated peaks is about 2.7% of the total data points. Fig. 2 shows a hologram function $\chi(\mathbf{k})$ after the peak elimination. The reconstructed atomic images are similar to those with a higher peak elimination threshold, *e.g.* of 5% (not shown).

For the reconstruction of atomic images from the obtained hologram we use Barton's reconstruction formula (Barton, 1988),

$$\psi(\mathbf{r}) = \int \mathrm{d}\Omega_{\mathbf{k}}\, \chi(\mathbf{k}) \exp(-i\,\mathbf{k}\cdot\mathbf{r}). \qquad (3)$$

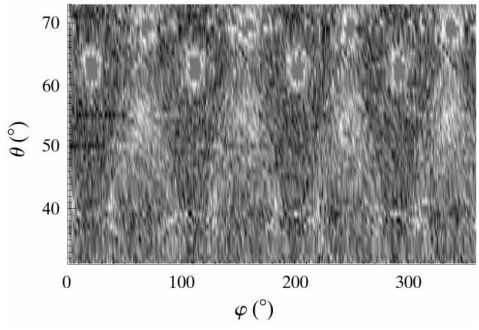


**Figure 2**
Normalized hologram $\chi(\mathbf{k})$ after peak elimination for a $Cu_3Au$ single crystal at an incident energy of 10.5 keV. The figure is shown in a linear grey scale (darker for larger values).

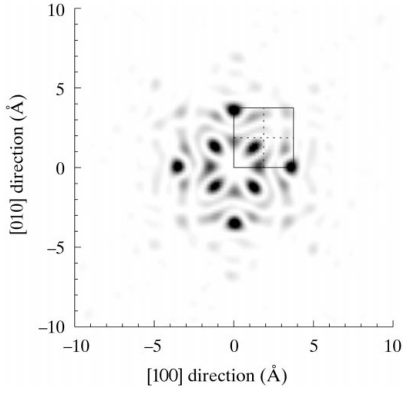


**Figure 3**
Holographic reconstruction of $Cu_3Au$ in the plane perpendicular to the $\varphi$ rotation axis and cutting through a fluorescing Cu atom. The reconstructed atomic intensity is shown in a linear grey scale (darker for higher intensity) without background cut-off. The coordinate origin is the position of a fluorescing Cu atom. The square with solid lines has a side length of the actual lattice constant, 3.75 Å, and the dashed lines are crossed at the centre of the square. They are drawn in order to indicate the actual positions of atoms.

In the actual data analysis the integral over the solid angle $\Omega_{\mathbf{k}}$ is replaced by the appropriate summation over measured points. In the following figures we show $|\psi(\mathbf{r})|^2$ as reconstructed atomic image intensity.

Fig. 3 shows the reconstructed image in the plane perpendicular to the $\varphi$ rotation axis ([001] direction) and cutting through a fluorescing Cu atom. Since two Cu atom positions with different atomic neighbourhoods are present in the $Cu_3Au$ crystal, one holographic reconstruction plane corresponds to an incoherent superposition of two lattice planes. This is because successive fluorescence events are mutually incoherent. The reconstruction plane of Fig. 3 corresponds to a superposition of the (100) and (200) lattice planes.

In Fig. 3 the coordinate origin is the position of a fluorescing Cu atom, which does not image itself. The square with solid lines has a side length of the actual lattice constant, 3.75 Å. Note that the hologram was rotated in $\varphi$ in order to obtain the [100] and [010] directions in the reconstructed image parallel to the image axis. The adjustment was performed by comparison of the measured XSW peak pattern with the theoretically simulated XSW peak pattern.

Since the $Cu_3Au$ crystal has an f.c.c.-based structure, atoms exist at all corners of the square of side-length 3.75 Å and at the cross point of the two dashed lines at the face centre in Fig. 3. The nearest neighbours of a fluorescing Cu atom at the face centres and the next-nearest neighbours at the corners are clearly imaged. Four images corresponding to the next-nearest neighbours appear at almost correct positions, and peak at 3.6 Å from the coordinate origin. The peak positions of the nearest neighbours are shifted by ~1 Å closer towards the coordinate origin compared with the actual positions of the atoms. The obtained atomic image possesses a fourfold rotational symmetry to good approximation without symmetrization of the data.

In order to estimate the spatial resolution of atomic images, we show in Fig. 4 a one-dimensional section in the [010] direction and through the coordinate origin of Fig. 3.

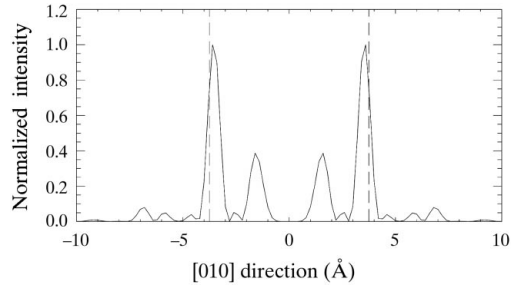


**Figure 4**
Section in the [010] direction and through the coordinate origin of Fig. 3. A reconstructed atomic image intensity $|\psi(\mathbf{r})|^2$ normalized the maximum intensity of the image Fig. 3 to unity is plotted. Dashed lines indicate the actual positions of atoms (3.75 Å from the origin).

The full width at half-maximum (FWHM) resolution of the next-nearest-neighbour images is ~0.7 Å.

For simplified cases the FWHM resolution of a reconstructed image can be calculated analytically (Tonner *et al.*, 1991; Saldin *et al.*, 1991). Let us consider a fluorescing atom at the coordinate origin and a neighbouring atom with isotropic form factor $f_a$ at $\mathbf{r}_a = (x_a, 0, 0)$. Then the scalar wave reciprocal hologram is given by

$$\chi(\mathbf{k}) = -(2r_e f_a/x_a)\cos(kx_a + \mathbf{k}\cdot\mathbf{r}_a), \qquad (4)$$

where $r_e$ is the classical electron radius, and $\mathbf{k} = (k_x, k_y, k_z)$ is the wavevector with size $k = |\mathbf{k}|$. If the hologram is measured in the upper hemisphere ($k_z \geq 0$) the reconstructed atomic image intensity in the line connecting the fluorescence atom and the neighbouring atom is given by

$$|\psi(x)|^2 = (2\pi r_e f_a/x_a)^2\Big(\{j_0[k(x-x_a)]\}^2 + \{j_0[k(x+x_a)]\}^2 + 2\cos(2kx_a)\, j_0[k(x-x_a)]\, j_0[k(x+x_a)]\Big), \qquad (5)$$

where $j_0(x) = \sin(x)/x$ is a spherical Bessel function. On the right-hand side of (5) the first term is an atomic image, the second term is a twin image and the third term is a cross-term of the atomic image and the twin image. At an energy of 10.5 keV the FWHM resolution of the atomic image estimated from (5) is ~0.5 Å. The value we obtained from the experimental analysis is within this theoretical limit.

Fig. 5 shows the reconstructed image in the plane which is half a lattice constant above the reconstruction plane of Fig. 3. Again the square with solid lines has a side length of the actual lattice constant, 3.75 Å. In this plane the actual positions of atoms are at intersection points of the square of side-length 3.75 Å with the dashed lines. Although the image contains more background than the image of Fig. 3, the highest peaks appear at almost correct nearest-neighbour positions, and the shifts from the actual positions are ~0.3 Å (Fig. 6).

Fig. 7 shows the reconstructed image parallel to the $\varphi$ rotation axis and cutting through a fluorescing Cu atom. By comparing Figs. 3 and 7 it is apparent that the resolution of reconstructed images is better for the plane perpendicular to the $\varphi$ rotation axis. The dependence of the resolution on reconstruction planes simply stems from the data region of the measurement (Tonner *et al.*, 1991; Saldin *et al.*, 1991). If we look onto the Ewald sphere from the top (along the $\varphi$ axis), the data region of the current experiment is rotationally symmetric and covers a wide area. On the other hand, if we look onto the Ewald sphere from the side (perpendicular to the $\varphi$ axis), the data region is limited to a small area.

In order to solve this problem we utilize the fourfold rotational symmetry and the mirror symmetry of the sample. In principle this symmetry information can be

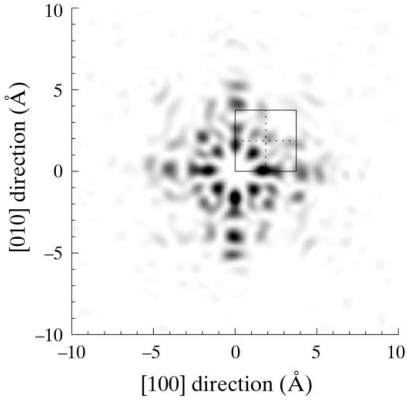


**Figure 5**
Holographic reconstruction of $Cu_3Au$ in the plane perpendicular to the $\varphi$ rotation axis and half a lattice constant above a fluorescing Cu atom. For comments on data presentation, see the caption of Fig. 3.

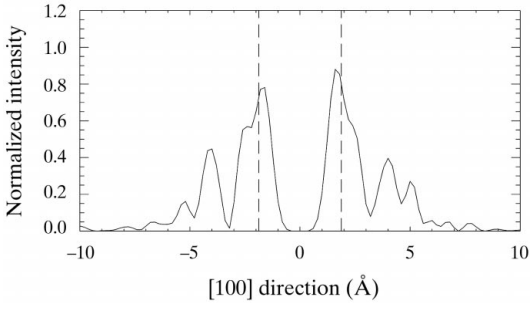


**Figure 6**
Section in the [100] direction and through the coordinate origin of Fig. 5. A reconstructed atomic image intensity $|\psi(\mathbf{r})|^2$ normalized the maximum intensity of the image Fig. 5 to unity is plotted. Dashed lines indicate the actual positions of atoms (1.875 Å from the origin).

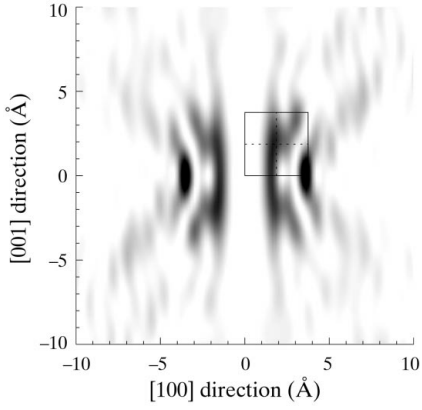


**Figure 7**
Holographic reconstruction of $Cu_3Au$ in the plane parallel to the $\varphi$ rotation axis and cutting through a fluorescing Cu atom. For comments on data presentation, see the caption of Fig. 3.

obtained from the XSW peak pattern. After averaging of $\psi(\mathbf{r})$ over symmetrically equivalent points in real space we obtain the three-dimensional image shown in Fig. 8. For a better visibility we omit background at a threshold of 50% of the maximum intensity. Six objects corresponding to the next-nearest neighbours of a fluorescing Cu atom are clearly visible. Their peak positions are at ~3.4 Å from the fluorescing Cu atom. The nearest neighbours are weaker and not visible, although they are imaged before symmetrization. The non-symmetrized $\psi(\mathbf{r})$ may have different phases at symmetrically equivalent points, and the symmetrization procedure may result in weaker intensities at some reconstruction points.

Finally, we show an XSW shape near a Bragg angle. In order to achieve a high count rate we installed an avalanche photodiode (APD) at a grazing angle of ~10°. The data from the APD cannot be used for the holographic reconstruction, because it does not have an energy resolution to select the Cu fluorescence lines. Fig. 9 shows an XSW shape near a Bragg angle measured by an APD. The width is mainly due to the divergence of the focused incident beam.

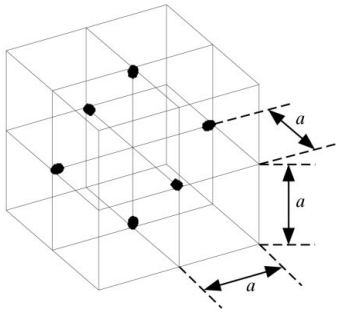


**Figure 8**
Three-dimensional holographic reconstruction of $Cu_3Au$ obtained after symmetrization (fourfold rotational symmetry and the mirror symmetry). Black dots are plotted at the positions where the reconstructed atomic image intensity $|\psi(\mathbf{r})|^2$ is larger than 50% of the maximum intensity. Cubes have a side length of the actual lattice constant $a$ = 3.75 Å. They are drawn in order to indicate the actual positions of atoms. The centre of the figure is the position of a fluorescing Cu atom. The images of the next-nearest neighbours of a fluorescing Cu atom peak at 3.4 Å from the centre. The nearest neighbours are weaker in intensity and not visible.

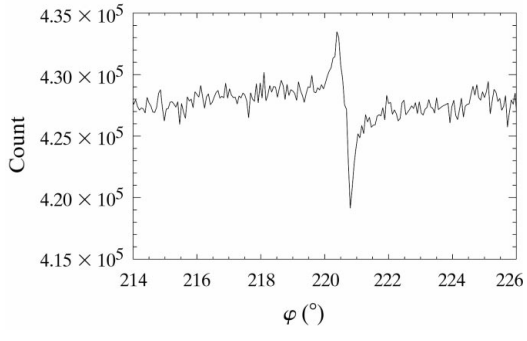


**Figure 9**
$\varphi$ scan at $\theta = 53°$ with an XSW shape near a Bragg angle. The data were obtained using an avalanche photodiode.

## 4. Conclusion and outlook

A reciprocal holography experiment on a $Cu_3Au$ single crystal was carried out with a new experimental set-up, which may be regarded as a pure reciprocal holography set-up. A continuous rotation of the sample during the fluorescence detection reduces the sensitivity to the source instability, and it also allows an efficient use of the available beam time. Atomic images from the holographic reconstruction were consistent with the actual $Cu_3Au$ structure even without symmetrization. By symmetrizing a reconstructed image we obtained a three-dimensional image of the $Cu_3Au$ atomic structure.

A highly oriented pyrolytic graphite (HOPG) (Grigoryeva *et al.*, 1990) has been used for the MEXH experiment in order to gain a higher count rate (Gog, Len *et al.*, 1996). A similar idea for a *pure* reciprocal holography set-up is to place a HOPG monochromator symmetrically about the $\varphi$ rotation axis.

The experimental set-up has the additional feature of a high angular resolution, which enables the measurement of XSW shapes near Bragg angles. This will be interesting for the study of defects. The immediate neighbourhood of the defect and its position relative to the undisturbed lattice farther away from it can be obtained from one data set. An interesting application would also be the study of dopants in semiconductor crystals (Hayashi *et al.*, 1998).

## References

Adams, B., Hiort, T., Kossel, E., Materlik, G., Nishino, Y. & Novikov, D. V. (1999). *Phys. Status Solidi B*, **215**, 757–771.
Adams, B., Hiort, T., Nishino, Y., Novikov, D. V., Kossel, E. & Materlik, G. (1998). *HASYLAB Annual Report 1998*, pp. 889–890. HASYLAB, DESY, Notkestrasse 85, D-22607 Hamburg, Germany.
Adams, B., Novikov, D. V., Hiort, T., Materlik, G. & Kossel, E. (1998). *Phys. Rev. B*, **57**, 7526–7534.
Barton, J. J. (1988). *Phys. Rev. Lett.* **61**, 1356–1359.
Bedzyk, M. J. & Materlik, G. (1985). *Phys. Rev. B*, **32**, 6456–6463.
Faigel, G. & Tegze, M. (1999). *Rep. Prog. Phys.* **62**, 355–393.
Gog, T., Bahr, D. & Materlik, G. (1995). *Phys. Rev. B*, **51**, 6761–6764.
Gog, T., Eisenhower, R. A., Menk, R. H., Tegze, M. & LeDuc, G. (1998). *J. Electron Spectrosc. Relat. Phenom.* **92**, 123–129.
Gog, T., Len, P. M., Materlik, G., Bahr, D., Fadley, C. S. & Sanchez-Hanke, C. (1996). *Phys. Rev. Lett.* **76**, 3132–3135.
Gog, T., Menk, R. H., Arfelli, F., Len, P. M., Fadley, C. S. & Materlik, G. (1996). *Synchrotron Rad. News*, **9**, 30–35.
Grigoryeva, I. G., Antonov, A. A. & Baryshev, V. B. (1990). *Synchrotron Rad. News* **3**, 15–17.

Hayashi, K., Yamamoto, T., Kawai, J., Suzuki, M., Goto, S., Hayakawa, S., Sakurai, K. & Gohshi, Y. (1998). *Anal. Sci.* **14**, 987–990.
Hiort, T., Novikov, D. V., Kossel, E. & Materlik, G. (2000). *Phys. Rev. B*, **61**, R830–R833.
Korecki, P., Korecki, J. & Karaś, W. (1999). *Phys. Rev. B*, **59**, 6139–6152.
Korecki, P., Korecki, J. & Ślezak, T. (1997). *Phys. Rev. Lett.* **79**, 3518–3521.
Nishino, Y. & Materlik, G. (1999). *Phys. Rev. B*, **60**, 15074–15083.
Novikov, D. V., Adams, B., Hiort, T., Kossel, E., Materlik, G., Menk, R. & Walenta, A. (1998). *J. Synchrotron Rad.* **5**, 315–319.
Saldin, D. K., Harp, G. R., Chen, B. L. & Tonner, B. P. (1991). *Phys. Rev. B*, **44**, 2480–2494.
Szöke, A. (1986). *AIP Conference Proceedings*, No. 147, edited by T. Atwood & J. Boker, pp. 361–367. New York: AIP.
Tegze, M. & Faigel, G. (1996). *Nature (London)*, **380**, 49–51.
Tegze, M., Faigel, G., Marchesini, S., Belakhovsky, M. & Chumakov, A. I. (1999). *Phys. Rev. Lett.* **82**, 4847–4850.
Tonner, B. P., Han, Z.-L., Harp, G. R. & Saldin, D. K. (1991). *Phys. Rev. B*, **43**, 14423–14433.